

Atomically thin synaptic devices for optoelectronic neuromorphic computation

Taimur Ahmed^{1,2,*}, Azmira Jannat,^{1,3,*} Vaishnavi Krishnamurthi¹, Thiha Aung¹, Aishani Mazumder¹, Ali Zavabeti^{1,4}, Nitu Syed¹, Torben Daeneke¹, Jian Zhen Ou¹, Akram Al-Hourani¹, and Sumeet Walia^{1,*}

¹School of Engineering, RMIT University, Melbourne VIC 3001, Australia

²Pak-Austria Fachhochschule: Institute of Applied Sciences and Technology, Haripur, 22620 Pakistan

³Research School of Physics, The Australian National University Canberra, ACT 2601, Australia

⁴Department of Chemical Engineering, The University of Melbourne Parkville, VIC 3010, Australia

*Correspondence to: taimurahmad1@gmail.com, azmira.jannat@anu.edu.au, sumeet.walia@rmit.edu.au

Abstract

Imaging sensors with inbuilt processing capability are expected to form the backbone of low-latency and highly energy efficient artificial vision systems. A range of emerging atomically thin materials provide opportunities to exploit their electrical and optical properties for human vision and brain inspired functions. Here, we report atomically thin nanosheets of β - In_2S_3 which exhibit inherent persistent photoconductivity (PPC) under ultraviolet and visible wavelengths. This PPC effect enables β - In_2S_3 based optoelectronic devices to optically mimic the dynamics of biological synapses. Based on the material characterisations, the PPC effect is attributed to the intrinsic defects in the synthesised β - In_2S_3 nanosheet. Furthermore, the feasibility of adopting these atomically thin synaptic devices for optoelectronic neuromorphic hardware is demonstrated by implementing a convolutional neural network for

This is the author manuscript accepted for publication and has undergone full peer review but has not been through the copyediting, typesetting, pagination and proofreading process, which may lead to differences between this version and the [Version of Record](#). Please cite this article as [doi: 10.1002/admt.202201772](https://doi.org/10.1002/admt.202201772).

image classification. As such, the demonstrated atomically thin nanosheets and optoelectronic synaptic devices provide a platform for scaling up complex vision-sensory neural networks, which can find many promising applications for multispectral imaging and neuromorphic computation.

Introduction

Two-dimensional (2D) semiconductors are strongly emerging as contenders for next-generation optoelectronic image processing and edge computing devices.^[1-5] Imaging combined with artificial neural networks is an emerging powerful technology for classification tasks in biomedical imaging and industrial manufacturing, as a couple of examples. Pre-processing images within the hardware can alleviate data streaming load, improve bandwidth budget and reduce latency and power consumption.^[1,6] These advantages have driven the development of optoelectronic sensors that combine sensory and computational functionalities in the same devices.^[7-10]

Among the prominently studied materials is indium sulphide (In_2S_3), an n-type non-layered post-transition metal chalcogenide.^[11-14] Recently, memory transistors based on In_2S_3 flakes (>5 nm) and thin films (>60 nm) with optical tunable resistance states and gate-tunable synaptic plasticity are reported.^[15] The thin films are synthesized by physical vapor deposition where In_2S_3 flakes grow and merge together to form thin films with grain boundaries. It is well reported that the orientation and distribution of grain boundaries in 2D materials remain random and uncontrolled for device application.^[16,17] This may compromise the scaling of devices and cause high power consumption during device operation.

While the conventional exfoliation and deposition techniques have been highly challenging to obtain atomically thin nanolayers of 2D semiconductors, we have used the unique liquid metal van der Waals (vdW) synthesis strategy to obtain unit cell thick nanosheets of In_2S_3 .^[11,18-20] Furthermore, for the first time, we have explored optoelectronic characteristics of atomically thin $\beta\text{-In}_2\text{S}_3$ nanosheets (~3 nm) for mimicking the rudimentary

operations of a biological synapse. The intrinsic vacancies and defects in the β - In_2S_3 crystal structure lead to the persistent photoconductivity, which has aided in formulating an artificial optoelectronic synaptic device. The demonstrated optoelectronic neuromorphic devices are able to mimic synaptic functions such as paired-pulse facilitation (PPF) and spatiotemporal spike-duration-dependant-plasticity (SDDP). Additionally, we have mimicked the Hebbian synaptic learning rule through spike-time-dependant-plasticity (STDP) using a multi-synaptic system. Finally, we demonstrate that our optoelectronic neuromorphic devices can be deployed for capturing images and a convolutional neural network (CNN) can be subsequently used for classification tasks.

Results and discussion

Large-scale 2D indium sulphide (In_2S_3) nanosheets are synthesised with a thickness down to a single unit to few unit cells by adapting a liquid metal-based synthesis method.^[11-19-21-22] The synthesis path follows a two-step procedure, consisting of removal of the oxide skin from molten indium and the subsequent sulfurization reaction at an elevated temperature in a tube furnace, under a constant nitrogen flow (see Methods for detail). Post-transition metals such as Ga, In, Sn, and their alloys undergo self-limiting Cabrera–Mott oxidation in their liquid state in the range of room temperature to low temperature, facilitating the growth of atomically thin interfacial oxides.^[21-23] These surface oxides can be easily delaminated onto the substrate in large-area nanosheets due to a very low adhesion to the bulk liquid metal. As such, atomically thin indium oxide nanosheets are extracted onto the SiO_2/Si substrates from the molten indium metal surface following a van der Waals printing method.^[21] Subsequently, the printed nanosheets are then transform to indium sulphide by sulfurization at 350 °C. Figure 1a shows an optical image of a representative nanosheet with the coverage

over a large area on the SiO₂/Si substrate. The topological atomic force microscope (AFM) scans (**Figure 1b**) are utilized to measure the morphology of the nanosheet. *Inset of Figure 1b* shows the typical AFM height profile measured around 3.2 nm at the edge of a representative as-synthesised nanosheet. **Figure 1c** shows an optical photograph of a representative device, fabricated as an artificial synapse (see Materials and Methods for fabrication details).

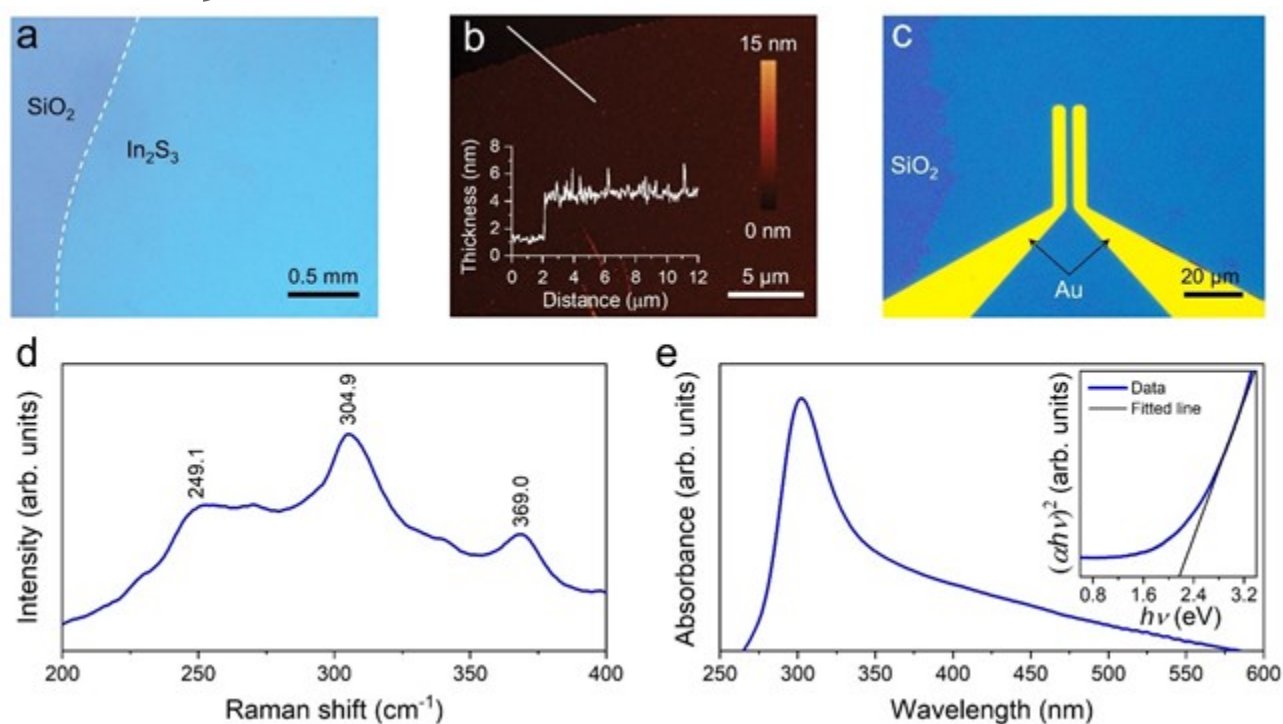


Figure 1. Optical and morphological characterisation of In₂S₃ nanosheets. (a) Optical image of a synthesised In₂S₃ nanosheet on SiO₂/Si substrate showing homogeneity over a large area. (b) A representative topological AFM scan at the edge of a nanosheet. Inset: Height profile of the nanosheet measured along the line indicative line in the AFM image. (c) Optical photograph of a fabricated device on the synthesised material. (d) Raman spectrum and (e) UV-vis optical absorbance of the In₂S₃ nanosheet on a SiO₂/Si substrate. Inset: Tauc plot extracted from the optical absorbance.

This article is protected by copyright. All rights reserved.

To assess the chemical structure of the printed nanosheets, Raman spectroscopic analysis is performed. **Figure 1d** shows Raman spectrum collected with a laser excitation of 532 nm on a few unit-cells thick In_2S_3 nanosheet (about 5-8 nm thick). The Raman peaks at 249.1, 304.9, and 369 cm^{-1} consists of A_1^g mode which matches with the previous reports for the thin cubic $\beta\text{-In}_2\text{S}_3$ nanosheet.^[12,24] For the optoelectronic applications, it is necessary to characterise the wavelength dependent optical absorbance of the In_2S_3 nanosheets. As such, optical absorbance measurements are performed in the ultra-violet to visible wavelength range. **Figure 1e** shows the absorbance profile of a representative In_2S_3 nanosheet on a SiO_2/Si substrate. The absorbance characteristic profile clearly shows that the In_2S_3 nanosheet exhibits maximum optical absorbance in UV with maximum peak centred at 302 nm. The optical absorbance is further analysed to calculate optical bandgap of the In_2S_3 nanosheets. The inset of the **Figure 1e** shows the Tauc plot where direct optical bandgap of ~ 2.17 eV is calculated by an extrapolated linear fit. These optical characterisations are utilised to exploit the optoelectronic applications of atomically thin In_2S_3 nanosheets for optically imitating biological synapses and neural network.

To study the electronic and optoelectronic properties of In_2S_3 nanosheets, devices in a phototransistor configuration are fabricated on SiO_2/Si substrates where highly conductive Si substrate (resistivity of <0.005 ohm-cm) is acting as a back gate. **Figure 2a** shows a schematic of a fabricated optoelectronic device on atomically thin In_2S_3 nanosheet where optical sources with different wavelengths are illuminated above the channel. The electronic and optoelectronic characterisations are performed on the In_2S_3 phototransistors (see Figure S1 in Supporting Information). Herein, we focus on the photoresponse of In_2S_3 nanosheets under different UV and visible wavelengths, and its implication for imitating

biological synaptic functions for optoelectronic neuromorphic computation. As such, fabricated In_2S_3 phototransistors are implemented as artificial optoelectronic synaptic devices where the active channel of In_2S_3 imitates as a synaptic cleft for transmitting the neurotransmitters and crystal defects in In_2S_3 optically enable synaptic dynamics. The modulation in conductance of In_2S_3 nanosheet, through electrical and optical stimuli/pulses, is read-out as postsynaptic current (PSC) and is related to the synaptic weight change/update. **Figure 2b** shows the normalised transient photoresponse of a representative In_2S_3 phototransistor under three consecutive illumination pulses of 285, 365 and 455 nm wavelengths with the pulse width of 2 seconds, power density of 3 mW/cm^2 and time interval of 20 seconds, measured with a constant drain-source voltage (V_{DS}) of 100 mV and without applying a gate voltage (i.e., $V_{\text{G}} = 0 \text{ V}$). Under the same experimental conditions, a higher photoresponse is measured under 285 nm as compared to 365 and 455 nm wavelengths which can be attributed to the highest optical absorbance of the In_2S_3 nanosheets closer to 285 nm (maximum absorbance peaks at $\sim 300 \text{ nm}$, **Figure 1e**). This indicates that under the optical pulses of wavelengths ($< 570 \text{ nm}$) with energies higher than the In_2S_3 energy bandgap ($> 2.17 \text{ eV}$), excess photoexcited electrons are generated owing to the band-to-band transition. Interestingly, regardless of the illuminating wavelength In_2S_3 exhibits slow recovery of the photocurrent after the optical illumination is turned off. This effect in In_2S_3 can be attributed to the trapping/de-trapping of photoexcited carriers at indium vacancies and defects in the nanosheets, as discussed below. The photoresponse of the In_2S_3 synaptic devices is further characterised for different wavelengths and experimental conditions (see Figure S2 in Supporting Information). Furthermore, another aspect of synaptic devices that needs to be considered is the device-to-device variability which may arise from the random nature of

trap density in a low dimensional material and nano-scale device variation in fabrication processes. As such, variations in the photoresponse of our In₂S₃ synaptic devices is evaluated under 285, 365 and 455 nm wavelengths. Photoresponse of at least five different synaptic devices is measured under similar experimental condition and a variation of <8% is calculated (see Figure S7 in Supporting Information).

X-ray photoelectron spectroscopy (XPS) is used to assess the elemental composition and stoichiometry of the as-prepared In₂S₃ nanosheet on SiO₂/Si substrate. **Figures 2c,d** show In3*d* and S2*p* core spectra, respectively. The In3*d* peaks are split into binding energies for the 3*d*_{5/2} at 444.8 eV and 3*d*_{3/2} at 452.4 eV with a ΔE of 7.6 eV. The S2*p* orbital (**Figure 2d**) splits into 2*p*_{3/2} at the binding energy of 161.6 eV and 2*p*_{1/2} at the binding energy of 162.9 eV with 1.1 eV of spin-orbit splitting. The binding energy values for In and S are well aligned with the previously published results of the β-In₂S₃.^[25-27] However, due to the low temperature conversion of In₂O₃ to β-In₂S₃, there are traces of excess sulphur deposited on the β-In₂S₃ nanosheets. In **Figure 2d**, two additional S peaks are observed at around 163.9 and 164.8 eV which are ascribed to the bridging S atoms bonded with In atoms, possibly indicates the formation of the highly defective structure.^[28-30] Furthermore, the β-In₂S₃ exhibits defected spinel (cubic and tetragonal) structure having a high concentration of vacancies on tetrahedral anion sites and defect states are introduced by the high-density vacant sites.^[31]

To further characterise the morphology and investigate the crystallographic properties of the In₂S₃ nanosheet, low-resolution transmission electron microscopy (TEM) and high-resolution TEM (HRTEM) are carried out. **Figure 2e** displays the low-magnification TEM

image of a typical In_2S_3 nanosheet transferred onto a carbon TEM grid. The HRTEM image and the corresponding selected area electron diffraction (SAED) pattern are presented in **Figure 2f** and **2g**. Both HRTEM and SAED analysis confirm the crystalline nature of the synthesized In_2S_3 with a lattice spacing of ~ 0.31 nm, diffraction patterns corresponding to the (206) planes of cubic In_2S_3 .^[25,26] Additionally, highlighted (white circles) area on the HRTEM image (**Figure 2f**) confirms the presence of the randomly distributed defects in the $\beta\text{-In}_2\text{S}_3$ nanosheet. As such, our as-synthesised $\beta\text{-In}_2\text{S}_3$ nanosheets can be considered as a quasi-ternary compound of a unit cell with In, S, and various disorders and vacancies.^[12,27] Disorder and vacancies in the as-synthesised $\beta\text{-In}_2\text{S}_3$ nanosheets are further confirmed from the scanning tunnelling microscopy (STM) measurements (Figure S3 in Supporting Information), which also supports HRTEM results.

Author Manuscript

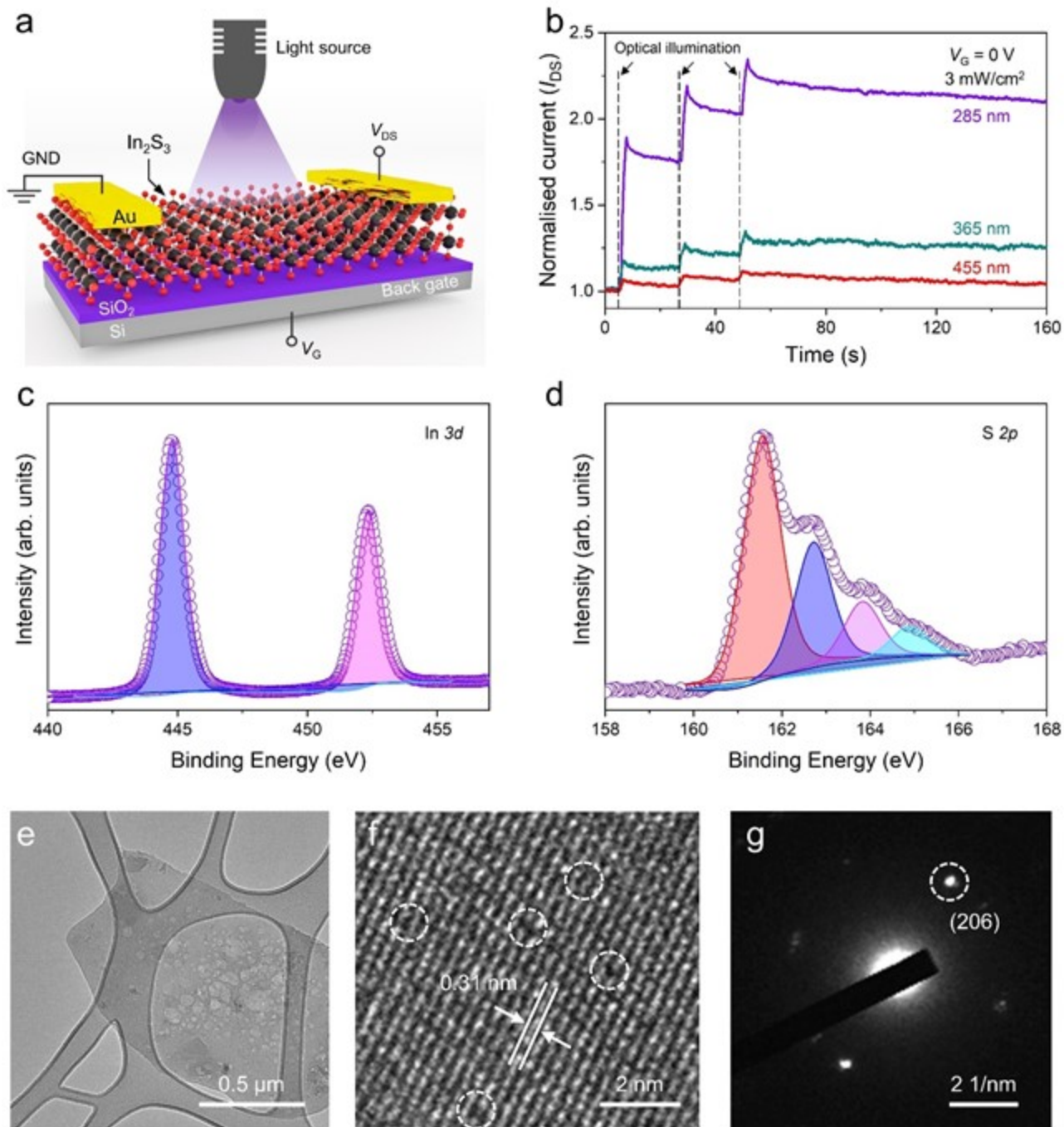


Figure 2. Photoresponse of optoelectronic device and compositional characterisation of In₂S₃ nanosheets. (a) Schematic illustration of an In₂S₃ optoelectronic device, fabricated on SiO₂/Si substrate as a phototransistor. (b) Normalised transient photoresponse of In₂S₃ nanosheet under the optical illumination of 285, 365 and 455 nm pulses with pulse width of 2 s and power density of 3 mW/cm². The photocurrent is measured between drain and source (I_{DS}) under a constant drain-source voltage (V_{DS}) of 100 mV and in the absence of gate voltage (V_G). X-ray photoelectron

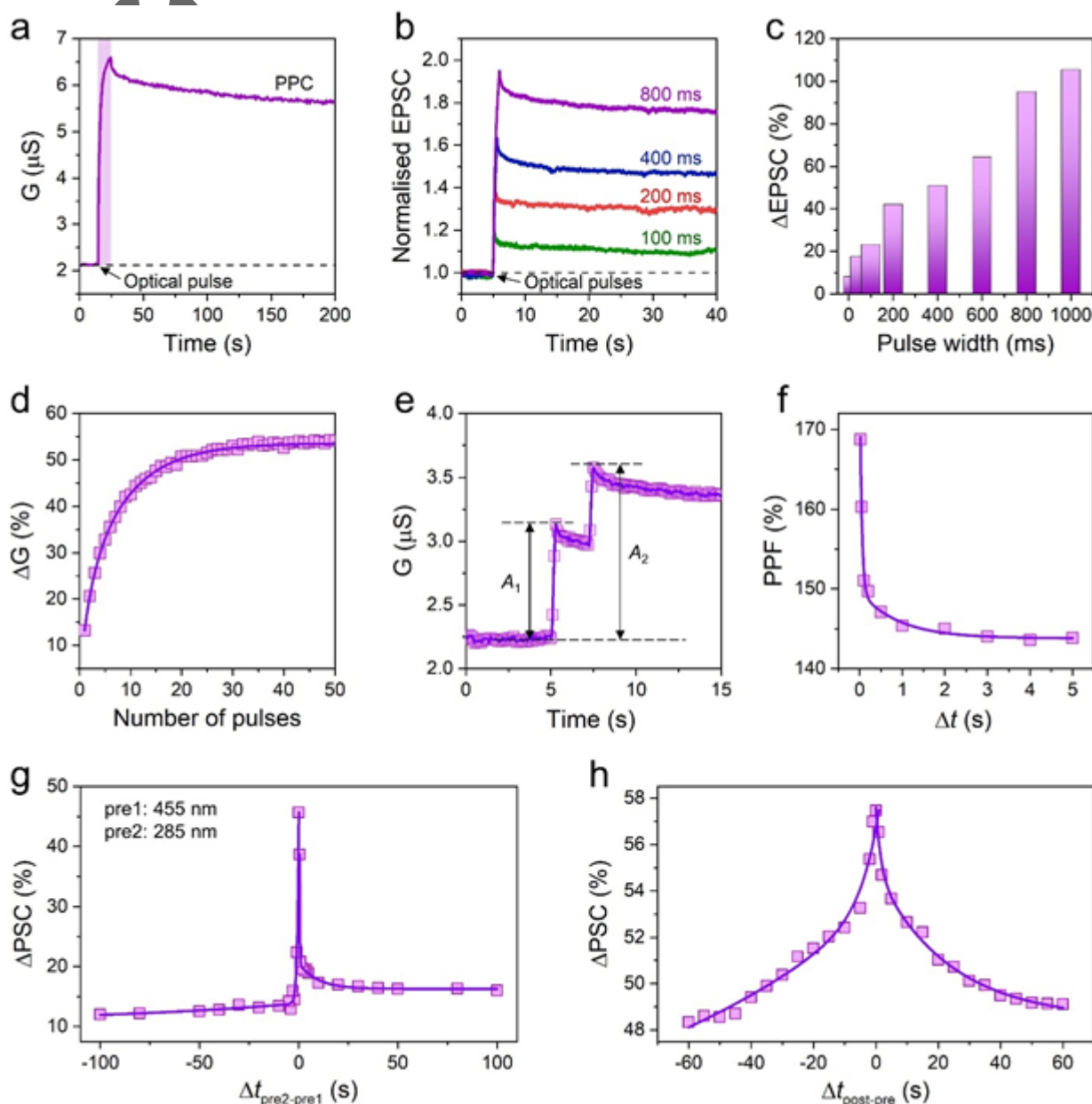
This article is protected by copyright. All rights reserved.

spectroscopy (XPS) core-level spectra of the as-synthesised cubic β - In_2S_3 nanosheet (c) In 3d and (d) S 2p. (e) Low-magnification transmission electron microscope (TEM) micrograph of the In_2S_3 nanosheet transferred on the carbon TEM grid. (f) High resolution TEM micrograph of β - In_2S_3 nanosheet. Circles highlighting random defects in the nanosheet. (g) Corresponding selected area electron diffraction pattern collected from the In_2S_3 nanosheet.

Figure 3a shows the transient photoresponse of In_2S_3 under a 5 s pulse of 285 nm wavelength (3 mW/cm^2), the slow recovery ($>10^4 \text{ s}$) of conductance (G) after the illuminating pulse is referred to the persistent photocurrent (PPC).^[32-33] The observed PPC in In_2S_3 is harnessed for optical imitation of the synaptic plasticity. For brevity, a detailed characterisation of the optoelectronic dynamics for synaptic plasticity is performed by illuminating 285 and 455 nm wavelengths on In_2S_3 optoelectronic devices operating in two-terminal configuration, without gate voltage. Any combination of two wavelengths from 285, 365 and 455 nm can also be used to imitate these synaptic functions. In biological neurons, duration of consecutive stimuli is critical for the neural functions as it can significantly affect the modulation of synaptic response. By inducing a temporal excitatory post-synaptic current (EPSC) response, our In_2S_3 artificial optoelectronic synaptic devices are exploited to mimic the spike-duration-dependant plasticity (SDDP). It is worth mentioning that SDDP can facilitate the intellectual process of learning or forgetting depending on the type of temporal response obtained from the synaptic device.^[34] The normalised EPSC (**Figure 3b**) shows the SDDP behaviour of the In_2S_3 synaptic devices when exposed to varying spike durations of optical pulses under the influence of 285 nm wavelength and at a power intensity of 3 mW/cm^2 .

Figure 3c shows the change in EPSC (ΔEPSC) for varying pulse widths, which reveals an

increasing change in magnitude for increasing spike durations. This can be attributed to the generation of photocarriers in In_2S_3 for a particular spike duration where a longer optical spike width causes higher photocarriers, thereby leading to a comparatively high EPSC change in magnitude.^[19] As such, depending on the photocurrent generated for a particular spike duration, varied synaptic weights can be obtained to achieve the SDDP behaviour.



This article is protected by copyright. All rights reserved.

Figure 3. Optoelectronic imitation of synaptic plasticity and synaptic learning. (a) Transient conductance of the In₂S₃ optoelectronic device in response to a 5 s pulse of 285 nm wavelength illuminated at the power intensity of 3 mW/cm². (b) Normalised EPSC in response to different 285 nm optical spike-duration ranging from 100 to 800 ms. (c) Bar chart of spike duration-dependent change in EPSC under 285 nm wavelength at 3 mW/cm². (d) Change in conductance as a function of number of optical pulses with the fixed pulse width of 500 ms and power intensity of 2 mW/cm². (e) Transient conductance in response to the pair of consecutive optical pulses with a time interval of 5 s. A_1 and A_2 represent the change in conductance at first and second optical spike, respectively. (f) Pair pulse facilitation (PPF) index as a function of time interval between consecutive 285 nm pulses. (g) Spatiotemporal change in PSC as a function of time interval between 455 nm and 285 nm optical pulses as pre1 and pre2 at 6 mW/cm² and 2 mW/cm² and a pulse width of 40 ms, respectively. (h) Change in synaptic weight as a function of time difference between post- and presynaptic pulses of 285 nm at 2 mW/cm².

Frequent administration of excitatory responses, in connected neurons, leads to the strengthening of memory, which can aid in attaining the psychological learning experience.^[35] This has been achieved by subjecting our In₂S₃ artificial optoelectronic synaptic devices to a train of identical presynaptic optical pulses. By applying a set of optical pulses (50 in this case) with a pulse width of 500 ms and power intensity of 2 mW/cm² under a 285 nm wavelength excitation, increasing values of EPSC are obtained for growing pulse numbers (**Figure 3d**). Also, though a fast-learning process accompanied the initial stage of rehearsal stimulations, it was accompanied by a gradual saturation of the EPSC response with increasing pulse numbers. As such, it implicates the need for fewer rehearsal stimulations to retain memory while enduring a continuous learning process.^[36] The learning behaviour of our device was fitted using an exponential growth function, $y = y_0 + A \cdot \exp\left(\frac{N}{\tau_1}\right)$, where τ_1 is the learning time, N is the number of presynaptic spikes, A is the initial facilitation magnitude in the learning process and y_0 is the resting facilitation magnitude (**Figure 3d**).

This article is protected by copyright. All rights reserved.

The dynamic synaptic plasticity is imitated by illuminating the In₂S₃ optoelectronic synaptic devices with two consecutive excitatory synaptic spikes of the same pulse width with a certain time delay between them. It is observed that the change in device conductance is more significant for the second optical spike (**Figure 3e**). This phenomenon is called paired-pulse facilitation (PPF),^[36] one of the forms of synaptic plasticity, which can interpret temporal information such as visual and aural signals.^[37] Here, the attained post-synaptic weight relies heavily on the time interval between the consecutive synaptic pulses. **Figure 3e** shows the change in conductance for two identical excitatory optical pulses with the pulse width of 200 ms, power intensity of 3 mW/cm² and the time interval (Δt) of 2 s. Upon the excitation of the second synaptic pulse, it is observed that the same pulse width leads to a relatively higher EPSC, i.e., the photocurrent obtained by the second optical pulse (A_2) is higher than the first optical pulse (A_1). Furthermore, to quantify EPSC induced PPF, the PPF index ratio (A_2/A_1), measured between the amplitude of the second spike and the first spike, is extracted and plotted as a function of time interval ranging between 20 ms and 5 s in **Figure 3f**. Finally, the extracted PPF indexes showing a bi-phase behaviour as fitted using a double exponential function, $y = y_0 + A_1 \cdot \exp\left(\frac{-\Delta t}{\tau_1}\right) + A_2 \cdot \exp\left(\frac{-\Delta t}{\tau_2}\right)$, where Δt is the time interval between two consecutive optical pulses, τ_1 and τ_2 are the fast and slow decay times and A_1 and A_2 are the facilitation magnitudes of the paired-pulses, respectively.

In biological synapses, the residue of Ca²⁺ ions from the first spike causes an overall increase in the Ca²⁺ levels after triggering the second spike. However, with an increasing time interval between the first and the second spike, a gradual decay in the residual Ca²⁺ forms after the excitation of the first spike which leads to a less change in EPSC.^[37] Analogous to the

residual Ca^{2+} ions in a biological synapse, the PPF behaviour in an artificial optoelectronic synapse can be explained concerning the generation and recombination of photocarriers. When the second optical spike is excited within a shorter time interval of the first spike, the generated electron-hole pairs undergo a shorter relaxation time, causing a carrier augmentation which ultimately enhances the photocurrent and the EPSC response. But, at extended time intervals, the generated electron-hole pairs undergo a more extensive relaxation time where the magnitude of the photoresponse of the second optical spike becomes similar to that of the first spike due to the recombination of most of the carriers.^[19:38:39] Hence, significantly high PPF values are observed at short time intervals and low PPF values at long time intervals which saturates at a value close to 143%.

Developing a multi-synaptic system becomes essential to successfully imitate the functionalities of a biological neural network. Strengthening and weakening various synaptic connections within a neural network count heavily on the number of pulses and the triggering time interval between two or more pulses.^[40:41] With a focus on realising spatiotemporal multi-synaptic neural network, we use 455 nm and 285 nm as pre-synapse 1 and pre-synapse 2 at 6 mW/cm^2 and 2 mW/cm^2 and a pulse width of 40 ms, respectively. By simultaneously triggering pre-synapse 1 and pre-synapse 2 with time intervals between 0 and 100 s, the photogenerated carriers from the second spike are added to the photocarriers of the first spike, increasing the total magnitude of the final PSC leading to a spatiotemporal summation. This change in PSC however depends on the time interval between spikes. For example, by concurrently triggering pre-synapse 1 and pre-synapse 2 ($\Delta t_{\text{pre2-pre1}} = 0$), a maximum change in the magnitude of PSC is noticed, as shown in **Figure 3g**. Additionally, by increasing the $|\Delta t_{\text{pre2-pre1}}|$, the value of PSC decreases disproportionately. This observed

disproportionality in PSC with increasing the $|\Delta t_{\text{pre2-pre1}}|$ can be associated with the difference in generated photocurrent under two different synaptic stimuli i.e., 455 nm and 285 nm wavelengths which are considered as presynapse 1 and presynapse 2 stimuli, respectively.

The biological neurons exhibit Hebbian synaptic learning by controlling the timing between presynaptic action potentials and postsynaptic action potentials, also referred as spike-time-dependent-plasticity (STDP).^[42] Based on the experimental data collected from biological neurons, four ideal STDP functions are usually adopted in computation models.^[43] The STDP functions are defined by different spiking order or type of synapse – excitatory or inhibitory. For example, the synaptic weight change determined by timing difference between pre- and postsynaptic spikes and their stimulation order defines asymmetric STDP. On the other hand, the synaptic weight change determined only by timing difference between pre- and postsynaptic spikes defines symmetric STDP.^[40-44-46] In our In_2S_3 synaptic devices, symmetric STDP is optically emulated where two separate devices are fabricated on the same sample and interconnected for individual optical excitation. The synaptic weight between the presynaptic and postsynaptic neurons is altered by controlling the activation time between the interconnected neurons. The interconnected In_2S_3 synaptic devices, namely a pre-synaptic neuron and a post-synaptic neuron, are both illuminated with a wavelength of 285 nm, a pulse width of 40 ms and power intensity of 2 mW/cm². The synaptic weight change (ΔPSC) as a function of $(\Delta t_{\text{post-pre}})$ defined as $\Delta\text{PSC} = (\Delta\text{PSC}_{\text{post}} - \Delta\text{PSC}_{\text{pre}})/\Delta\text{PSC}_{\text{pre}}$ is plotted in **Figure 3h**. Regardless of the order in which the pre and post-synaptic spikes are stimulated, a symmetric change in synaptic weight is obtained, where ΔPSC is maximum when $|\Delta t_{\text{post-pre}}|$ has the minimum value, and ΔPSC symmetrically decreases with increasing $|\Delta t_{\text{post-pre}}|$. As

This article is protected by copyright. All rights reserved.

such, our In₂S₃ optoelectronic synaptic devices mimic the fundamental behaviour of Hebbian learning.

The electrical and optical energy consumption (E_{ele} and E_{opt} , respectively) of our In₂S₃ synaptic devices can be calculated by considering the current (I) generated in response to the stimuli pulses (of duration t), with illumination power (P_{opt}) in the case of optical pulse, measured at drain-source voltage (V_{DS}) and device area (D), i.e., $E_{\text{ele}} = I \times t \times V_{\text{DS}}$ and $E_{\text{opt}} = P_{\text{opt}} \times t \times D$.^[47] An optical pulse of 285 nm wavelength with a power of 0.3 mW cm⁻² and duration of 50 ms generates conductance change of >0.5% which can imitate synaptic functions under the V_{DS} of 10 mV across the device area of ~125 μm². So, the execution of synaptic function consumes E_{ele} of ~0.81 pJ and E_{opt} of ~1.8 fJ. **Table 1** compares the key characteristics of our In₂S₃ synaptic devices with the reported state-of-the-art electronic and optoelectronic 2D synaptic devices.

Although a few individual or interconnected phototransistors are enough to imitate most of the fundamental synaptic functions, large-scale image recognition, pattern classification and neuromorphic computation are contingent on the demonstration of neural operations in a large array of photo-responsive devices. Realization of photo-responsive array has been demonstrated on different large-area 2D materials,^[6] including mechanically exfoliated 2D materials.^[4] In this work, individual and a couple of interconnected In₂S₃ devices are used to undertake optoelectronic synaptic characterisation. Since atomically thin In₂S₃ nanosheets can be confidently synthesized on a large area (Figure 1a), pixel arrays can be developed by patterning nanosheets with different dry ion etching and wet etching techniques.^[48]

To further demonstrate the adoptability of our In_2S_3 optoelectronic synaptic devices for the artificial intelligence hardware, we classify Canadian Institute for Advanced Research (CIFAR-10) dataset using convolutional neural network (CNN) architecture.^[1:49:50] Since the introduction of CNN model for such devices, it has achieved a unprecedented success over conventional neural networks in resolving computer vision challenges such as image segmentation and object detection. A CNN model has features of segregate layers, modularised kernels and combine weight sharing and sparse connectivity to perform fast and accurate feature recognition with far fewer weights than conventional networks.^[51:52] Herein, the adopted CNN architecture is composed of input images of 10 different classes with the size of $32 \times 32 \times 3$ and three convolutional layers (**Figure 4a**).^[53] Each convolutional layer with kernel of 3×3 weights is followed by ReLu activation function and maxpooling layer to avoid overfitting. Then the output of third maxpooling layer is connected to the fully connected layer and classify the result as output (See Supporting Information Figure S4-S6 for detail). During the training phase of neural network for 50,000 images, the weights kernel in the convolutional layer is updated to classify the result with high accuracy. In hardware neural network using In_2S_3 optoelectronic synaptic devices, the weight is assigned as multi-level conductance states (**Figure 4b**) and the weight update during training will be controlled by optical pulses (of 280 nm wavelength and pulse width of 0.2 s) and electrical pulses (of -0.5 V amplitude and pulse width of 0.2 s) for the long-term potentiation (LTP) and long-term depression (LTD), respectively. An ideal device exhibits a linear weight update which is proportional to the number of optical/electrical pulses for potentiation/depression, respectively. However, the LTP and LTD characteristics of our In_2S_3 optoelectronic synaptic devices are nonlinear which may deviate the weight change from the ideal linear weight

This article is protected by copyright. All rights reserved.

change.^[54] As such, the nonlinearity of conductance change effects the accuracy of the neural network during training.^[55] To indicate the impact of nonlinearity, behaviour model is used to evaluate the linearity of the weight update by the following equations,^[47:55:56]

$$G_{LTP} = B \left(1 - e^{-\frac{P}{A}} \right) + G_{min} \quad (1)$$

$$G_{LTD} = -B \left(1 - e^{-\frac{P-P_{max}}{A}} \right) + G_{max} \quad (2)$$

$$B = \frac{G_{max} - G_{min}}{1 - e^{-\frac{P_{max}}{A}}} \quad (3)$$

where G_{LTP} and G_{LTD} are the LTP and LTD conductance, respectively. G_{max} , G_{min} , P and P_{max} are maximum and minimum conductance, pulse number and maximum pulse number, respectively, and are directly extracted from the experimental data (**Figure 4b**). A represents the nonlinearity parameter which controls the nonlinear behaviour of weight update. For the given experimental data, the nonlinearity value of LTP and LTD values of 3.8 and 2.2, respectively, are calculated.

The CNN is simulated using the optoelectronic characteristics of our In_2S_3 optoelectronic synaptic devices and we compare the classification accuracy during training with ideal and experimental data for 250 epochs. **Figure 4c** shows the classification accuracy where the performance of neural network drops due to nonlinearity in experimental data at the early epoch. This can be associated with the same polarity of nonlinearity value for LTP and LTD.^[57:58] However, the classification accuracy exceeds 80% after 150 epoch, as after multiple training cycles the nonlinear weight update is compensated. The classification accuracy of our CNN model based on optoelectronic In_2S_3 synaptic devices is comparable to

the reported CNN models based on different 2D materials. A comparison of different 2D materials based neural networks and their performance is presented in Table 1.

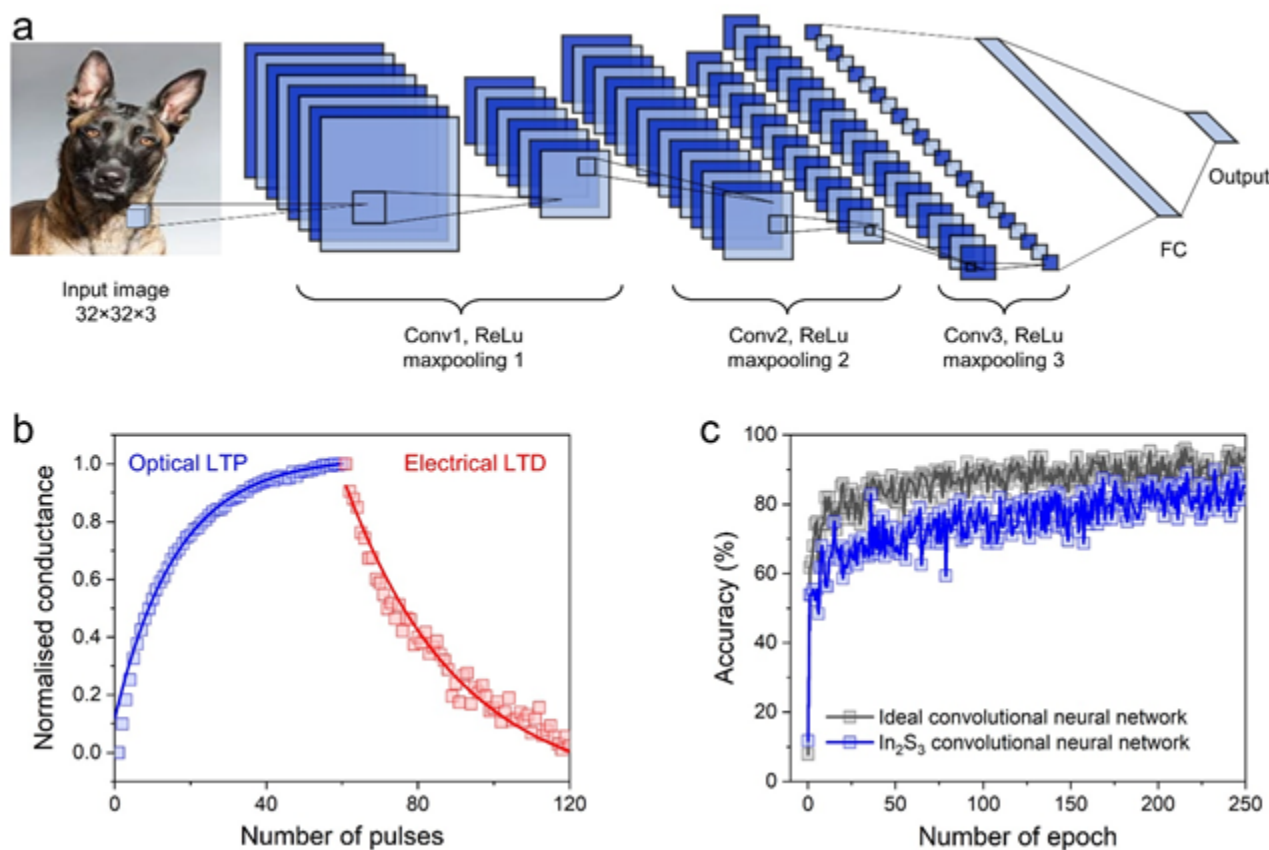


Figure 4. Optoelectronic convolutional neural network based on atomically thin In₂S₃ optoelectronic synaptic devices. (a) Schematic illustration of CNN architecture for the CIFAR-10 dataset. (b) Weight update LTP/LTD characteristics of In₂S₃ optoelectronic synaptic devices. For optical LTP weight update, short pulses of 280 nm wavelength at power density of 3 mW/cm² with the pulse width of 200 ms are illuminated on the In₂S₃ synaptic devices. Short voltage pulses with the amplitude of -0.5 V and duration of 200 ms are applied for electrical LTD weight update. (c) Comparison of classification accuracies of CNN for an ideal device and In₂S₃ optoelectronic synaptic device.

Table 1. Comparison of key features of our In₂S₃ synaptic devices with reported synaptic devices. Abbreviations — CNN: Convolutional neural network, NG: Not given, QDs: Quantum dots, CNT: Carbon nanotubes, UCNPs: upconverting nanoparticles

This article is protected by copyright. All rights reserved.

Material	Optical Pulses (wavelength)	Electrical Pulses	Max. PPF index	STDP	Neural network simulations (Accuracy)	Presynaptic spike time (ms)	Power consumption (pJ)	Ref.
In ₂ S ₃	Potentiation (285, 365, 455 nm)	Habituation	169%	Yes	CNN (>80%)	50	1.8×10 ⁻³ (optical) 0.81 (electrical)	This work
ZnO	Potentiation (365 nm)	--	170%	Yes	NG	70	87.5	[19]
ReS ₂	Potentiation (656 nm)	Habituation	132%	NG	CNN (89% - 92%)	50	12×10 ⁴ (reading) 0.56 (writing)	[47]
WSe ₂ /h-BN	Potentiation (405, 532, 655 nm)	Habituation	NG	Yes	ANN/ONN (90%)	10	0.532	[44]
Black Phosphorus	Potentiation (280, 660 nm) & Habituation (365 nm)	Potentiation & Habituation	285% (280 nm) 155% (365 nm)	Yes	NG	10 ²	~3.5 (optical) ~9.24×10 ² (electrical)	[34]
	Program (780 nm)	Program & Reset	NG	NG	CNN (92%)	NG	NG	[1]
	--	Potentiation & Habituation	NG	Yes	NG	10	NG	[59]
UCNPs-MoS ₂	Program (980 nm)	Erase	191%	NG	ANN (70%)	100	NG	[60]

This article is protected by copyright. All rights reserved.

MoS ₂	Potential (455nm)	Potential & Habituation	206% (ionotronic mode) 165% (electronic mode)	Yes	NG	10.5	~4.8 (ionotronic mode) ~1.3×10 ⁴ (electronic mode)	[61]
	Potential (310nm)	Habituation	120%	NG	NG	10 ³	NG	[62]
MoO ₃	--	Potential & Habituation	14%	NG	NG	1	9.6	[63]
WSe ₂ , NiPS ₃ , FePSe ₃	--	Potential & Habituation	290%	NG	NG	10 ⁻¹	3×10 ⁻² (WSe ₂)	[64]
CsPbBr ₃ QDs	Potential (365-660nm)	Habituation	130%	NG	NG	10 ³	1.4×10 ³	[65]
Graphene/CN T hybrid	Habituation (405, 532nm)	Potential	155%	NG	NG	5	NG	[66]
Graphene	--	Potential & Habituation	NG	Yes	NG	10	5×10 ⁻¹	[67]

Conclusion

In this study, we harnessed inherent persistent photocurrent of atomically thin In₂S₃ nanosheets to imitate photosensitive modulation of the synaptic weight in response to optical stimulations, thereby

This article is protected by copyright. All rights reserved.

successfully mimicking the dynamics of biological synapses, such as the EPSC, PPF, and LTP characteristics. The persistent nature of photocurrent under optical excitation is attributed to the trapping/de-trapping of photoexcited carrier at defects and indium vacancies. Finally, the synaptic functions are utilised to demonstrate the feasibility of applying In_2S_3 optoelectronic synapse devices in hardware for neuromorphic computation. Based on the optoelectronic data of our In_2S_3 devices, a convolutional neural network is simulated for the CIFAR-10 dataset which shows recognition rate of >80%.

Materials and Methods

Synthesis of In_2S_3 nanosheets: Large area 2D indium sulphide (In_2S_3) nanosheets were synthesised with a thickness down to a single unit to few unit cells by adapting a liquid metal-based synthesis method. In the first step, a piece of indium metal (purity: 99.99%, Roto Metal) was allowed to melt at 180 °C on a clean glass slide, using a hot plate inside a glove box with the oxygen concentration <100 ppm. Pre-existing native oxide layer was scraped off from the surface of molten indium metal with a glass Pasteur pipet. Subsequently, a clean 300 nm SiO_2/Si wafer (D&X Co., Ltd, Japan) was pre-heated at 180 °C and then brought in-contact with the surface of the molten indium metal. As such, a fresh indium oxide layer was printed on the surface of the wafer. In the second step, the printed indium oxide layer was sulphurised into In_2S_3 at 350 °C for 150 min by exposing the samples to sulphur vapours under a constant nitrogen flow.

Structural, Morphological and Optical Characterisation: The high-quality optical images were obtained using Upright Microscope BX1 LED Olympus equipped with a 5-megapixel colour camera and standard colour stream image acquisition software.

This article is protected by copyright. All rights reserved.

Thicknesses of the synthesised In_2S_3 nanosheets were measured by topographic scans on a Dimension-Icon AFM in ScanAsyst mode.

Thermo Scientific K-alpha XPS spectrometer equipped with a monochromatic $\text{Al K}\alpha$ source and a concentric hemispherical analyser were used to determine the chemical composition of the synthesised nanosheets. The analyser was operated with pass energy of 100 eV to record the core-level spectra and 50 eV to record the valance band spectra. A low-energy electron flood gun was utilized to remove surface charging effect of the synthesised material.

The HRTEM measurements were conducted using JEOL 2100F at 80 kV acceleration voltage. Raman spectra was collected using a Horiba Scientific LabRAM HR evolution Raman spectrometer. The samples were excited with a 4.5 mW, 532 nm lasers, and the measurements were conducted using a $50\times$ lens and 1800 lines/mm grating. STM was performed under ultra-high vacuum using Scienta Omicron model VT XA equipped with Matrix SPM control system.

The UV–vis absorbance spectra of the nanosheets were collected by CRAIC 20/30 XL UV–vis microspectrophotometer.

Device fabrication: The contact electrodes on top of the synthesised In_2S_3 nanosheets were patterned using a mask-less photolithography process using a Maskless Aligner MLA 150 (Heidelberg Instruments) and photoresist AZ 1512HS. The metal electrodes of Cr (purity: 99.999%, thickness: 10 nm) and Au (purity: 99.999%, thickness: 100 nm) were then deposited using electron beam evaporation and the lift-off of metal was achieved by immersing the samples in acetone for 20 minutes, followed by isopropyl alcohol cleaning and nitrogen blow dry steps.

This article is protected by copyright. All rights reserved.

Electrical and Optoelectronic Measurements: The electronic and optoelectronic measurements were conducted using a semiconductor parameter analyzer (Keithley 4200SCS) and Agilent 2912A source meter. All measurements were performed under dark conditions with exposure to only the selected illumination wavelengths in ambient environment. The optoelectronic measurements are performed under commercial non-polarised light-emitting diodes with illumination wavelengths of 285, 365 and 445 nm (Thorlabs, Inc.). The illumination power was measured and calibrated by a commercial UV-enhanced silicon photodetector (Newport Corporation). The illumination frequency, pulse count and pulse width of the light sources were controlled by a programmable microcontroller board.

Acknowledgements

This work was performed in part at the Micro Nano Research Facility at RMIT University in the Victorian Node of the Australian National Fabrication Facility (ANFF). SW acknowledges project support via Australian Research Council Discovery Project DP220100020. Authors also acknowledge the contribution of Mei Xian Low in rendering schematics.

References

- [1] S. Lee, R. Peng, C. Wu, M. Li, *Nat Commun* **2022**, 13, 1485.
- [2] Z. Zhang, S. Wang, C. Liu, R. Xie, W. Hu, P. Zhou, *Nat Nanotechnol* **2022**, 17, 27.
- [3] L. Pi, P. Wang, S.-J. Liang, P. Luo, H. Wang, D. Li, Z. Li, P. Chen, X. Zhou, F. Miao, T. Zhai, *Nat Electronics* **2022**, 5, 248.
- [4] X. Liu, F. Wang, J. Su, Y. Zhou, S. Ramakrishna, *Adv Func Mater* **2022**, 32, 2113050.
- [5] S. Batool, M. Idrees, S.-R. Zhang, S.-T. Han, Y. Zhou, *Nanoscale Horiz* **2022**, 7, 480.
- [6] L. Mennel, J. Symonowicz, S. Wachter, D. K. Polyushkin, A. J. Molina-Mendoza, T. Mueller, *Nature* **2020**, 579, 62.
- [7] F. Zhou, Y. Chai, *Nat Electronics* **2020**, 3, 664.

- [8] T. Wan, B. Shao, S. Ma, Y. Zhou, Q. Li, Y. Chai, *Adv Mater* **2022**, n/a, 2203830.
- [9] F. Liao, Z. Zhou, B. J. Kim, J. Chen, J. Wang, T. Wan, Y. Zhou, A. T. Hoang, C. Wang, J. Kang, J.-H. Ahn, Y. Chai, *Nat Electronics* **2022**, 5, 84.
- [10] H. Jang, H. Hinton, W.-B. Jung, M.-H. Lee, C. Kim, M. Park, S.-K. Lee, S. Park, D. Ham, *Nature Electronics* **2022**, 5, 519.
- [11] A. Jannat, Q. Yao, A. Zavabeti, N. Syed, B. Y. Zhang, T. Ahmed, S. Kuriakose, M. Mohiuddin, N. Pillai, F. Haque, *Mater Horizons* **2020**.
- [12] W. Huang, L. Gan, H. Yang, N. Zhou, R. Wang, W. Wu, H. Li, Y. Ma, H. Zeng, T. Zhai, *Adv Func Mater* **2017**, 27, 1702448.
- [13] J. Lu, J. Yao, J. Yan, W. Gao, L. Huang, Z. Zheng, M. Zhang, J. Li, *Mater Horiz* **2020**, 7, 1427.
- [14] F. Horani, E. Lifshitz, *Chem Mater* **2019**, 31, 1784.
- [15] Y. Zhao, D. Yu, Z. Liu, S. Li, Z. He, *IEEE Access* **2020**, 8, 106726.
- [16] V. K. Sangwan, D. Jariwala, I. S. Kim, K.-S. Chen, T. J. Marks, L. J. Lauhon, M. C. Hersam, *Nat Nanotechnology* **2015**, 10, 403.
- [17] V. K. Sangwan, H.-S. Lee, H. Bergeron, I. Balla, M. E. Beck, K.-S. Chen, M. C. Hersam, *Nature* **2018**, 554, 500.
- [18] T. Daeneke, P. Atkin, R. Orrell-Trigg, A. Zavabeti, T. Ahmed, S. Walia, M. Liu, Y. Tachibana, M. Javid, A. D. Greentree, *ACS Nano* **2017**, 11, 10974.
- [19] V. Krishnamurthi, T. Ahmed, M. Mohiuddin, A. Zavabeti, N. Pillai, C. F. McConville, N. Mahmood, S. Walia, *Adv Optical Mater* **2021**, 9.
- [20] K. A. Messalea, A. Zavabeti, M. Mohiuddin, N. Syed, A. Jannat, P. Atkin, T. Ahmed, S. Walia, C. F. McConville, K. Kalantar-Zadeh, N. Mahmood, K. Khoshmanesh, T. Daeneke, *Adv Mater Interfaces* **2020**, 7, 2001131.
- [21] A. Jannat, N. Syed, K. Xu, M. A. Rahman, M. M. M. Talukder, K. A. Messalea, M. Mohiuddin, R. S. Datta, M. W. Khan, T. Alkathiri, B. J. Murdoch, S. Z. Reza, J. Li, T. Daeneke, A. Zavabeti, J. Z. Ou, *ACS Nano* **2021**, 15, 4045.
- [22] K. A. Messalea, A. Zavabeti, M. Mohiuddin, N. Syed, A. Jannat, P. Atkin, T. Ahmed, S. Walia, C. F. McConville, K. Kalantar-Zadeh, N. Mahmood, K. Khoshmanesh, T. Daeneke, *Advanced Materials Interfaces* **2020**, 7, 2001131.
- [23] R. S. Datta, N. Syed, A. Zavabeti, A. Jannat, M. Mohiuddin, M. Rokunuzzaman, B. Yue Zhang, M. A. Rahman, P. Atkin, K. A. Messalea, M. B. Ghasemian, E. D. Gaspera, S.

- Bhattacharyya, M. S. Fuhrer, S. P. Russo, C. F. McConville, D. Esrafilzadeh, K. Kalantar-Zadeh, T. Daeneke, *Nat Electronics* **2020**, 3, 51.
- [24] A. Mumtaz, N. M. Mohamed, M. Mazhar, M. A. Ehsan, M. S. Mohamed Saheed, *ACS Appl Mater Interfaces* **2016**, 8, 9037.
- [25] W. Gao, W. Liu, Y. Leng, X. Wang, X. Wang, B. Hu, D. Yu, Y. Sang, H. Liu, *Applied Catalysis B: Environmental* **2015**, 176-177, 83.
- [26] D. Yu, Z. Zhuo, A. Wei, J. Liu, Y. Zhao, Z. Xiao, *Journal of Materials Science: Materials in Electronics* **2020**, 31, 18175.
- [27] A. Jannat, Q. Yao, A. Zavabeti, N. Syed, B. Y. Zhang, T. Ahmed, S. Kuriakose, M. Mohiuddin, N. Pillai, F. Haque, G. Ren, D. M. Zhu, N. Cheng, Y. Du, S. A. Tawfik, M. J. S. Spencer, B. J. Murdoch, L. Wang, C. F. McConville, S. Walia, T. Daeneke, L. Zhu, J. Z. Ou, *Mater. Horiz.* **2020**, 7, 827.
- [28] O. A. Carrasco-Jaim, R. Ahumada-Lazo, P. C. Clark, C. Gómez-Solis, S. M. Fairclough, S. J. Haigh, M. A. Leontiadou, K. Handrup, L. M. Torres-Martínez, W. R. Flavell, *Int. J. Hydrog. Energy* **2019**, 44, 2770.
- [29] H. Lin, L. Yang, X. Jiang, G. Li, T. Zhang, Q. Yao, G. W. Zheng, J. Y. Lee, *Energ. Environ. Sci.* **2017**, 10, 1476.
- [30] H. Lin, L. Yang, X. Jiang, G. Li, T. Zhang, Q. Yao, G. W. Zheng, J. Y. Lee, *Energy & Environmental Science* **2017**, 10, 1476.
- [31] W. Rehwald, G. Harbeke, *Journal of Physics and Chemistry of Solids* **1965**, 26, 1309.
- [32] M. Lee, W. Lee, S. Choi, J. W. Jo, J. Kim, S. K. Park, Y. H. Kim, *Adv. Mater.* **2017**, 29, 1700951.
- [33] H. Jang, C. Liu, H. Hinton, M. H. Lee, H. Kim, M. Seol, H. J. Shin, S. Park, D. Ham, *Adv Mater* **2020**, 32, e2002431.
- [34] T. Ahmed, S. Kuriakose, E. L. H. Mayes, R. Ramanathan, V. Bansal, M. Bhaskaran, S. Sriram, S. Walia, *Small* **2019**, 15, e1900966.
- [35] G. Du, W. Ma, T. Chang, P. Sheridan, W. D. Lu, *Adv Func Mater* **2015**, 25, 4290.
- [36] R. C. Atkinson, R. M. Shiffrin, in *Psychology of learning and motivation: Advances in research and theory*, Vol. 2 (Eds: K. W. Spence, J. T. Spence), Elsevier, New York **1968**, pp. 89.
- [37] D. Debanne, N. C. Guérineau, B. H. Gähwiler, S. M. Thompson, *J. Physiol.* **1996**, 491, 163.

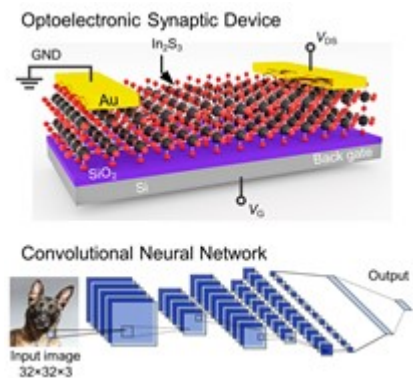
- [38] H. Tan, Z. Ni, W. Peng, S. Du, X. Liu, S. Zhao, W. Li, Z. Ye, M. Xu, Y. Xu, X. Pi, D. Yang, *Nano Energy* **2018**, 52, 422.
- [39] F. Guo, M. Song, M. C. Wong, R. Ding, W. F. Io, S. Y. Pang, W. Jie, J. Hao, *Adv Func Mater* **2021**, 32.
- [40] J. C. Magee, *Nat. Rev. Neurosci.* **2000**, 1, 181.
- [41] S. Qin, F. Wang, Y. Liu, Q. Wan, X. Wang, Y. Xu, Y. Shi, X. Wang, R. Zhang, *2D Materials* **2017**, 4.
- [42] S. Song, K. D. Miller, L. F. Abbott, *Nat Neurosci* **2000**, 3, 919.
- [43] L. F. Abbott, S. B. Nelson, *Nat Neurosci* **2000**, 3, 1178.
- [44] S. Seo, S. H. Jo, S. Kim, J. Shim, S. Oh, J. H. Kim, K. Heo, J. W. Choi, C. Choi, S. Oh, D. Kuzum, H. P. Wong, J. H. Park, *Nat. Commun.* **2018**, 9, 5106.
- [45] T. Ahmed, S. Walia, E. L. Mayes, R. Ramanathan, V. Bansal, M. Bhaskaran, S. Sriram, O. Kavehei, *Sci Rep* **2019**, 9, 1.
- [46] T. Ahmed, S. Kuriakose, E. L. H. Mayes, R. Ramanathan, V. Bansal, M. Bhaskaran, S. Sriram, S. Walia, *Small* **2019**, 15, 1900966.
- [47] S. Seo, J. J. Lee, R. G. Lee, T. H. Kim, S. Park, S. Jung, H. K. Lee, M. Andreev, K. B. Lee, K. S. Jung, S. Oh, H. J. Lee, K. S. Kim, G. Y. Yeom, Y. H. Kim, J. H. Park, *Adv Mater* **2021**, 33, e2102980.
- [48] Y. Wang, H. Tang, Y. Xie, X. Chen, S. Ma, Z. Sun, Q. Sun, L. Chen, H. Zhu, J. Wan, Z. Xu, D. W. Zhang, P. Zhou, W. Bao, *Nat Commun* **2021**, 12, 3347.
- [49] X. Peng, S. Huang, H. Jiang, A. Lu, S. Yu, *IEEE Transactions on Computer-Aided Design of Integrated Circuits and Systems* **2021**, 40, 2306.
- [50] M.-K. Kim, I.-J. Kim, J.-S. Lee, *Sci Advances* **2022**, 8, eabm8537.
- [51] D. Liu, H. Yu, Y. Chai, *Adv Intell Syst* **2020**, 3.
- [52] L. El Srouji, A. Krishnan, R. Ravichandran, Y. Lee, M. On, X. Xiao, S. J. Ben Yoo, *APL Photonics* **2022**, 7.
- [53] M. a. H. Courbariaux, Itay and Soudry, Daniel and El-Yaniv, Ran and Bengio, Yoshua, *arXiv* **2016**.
- [54] S. H. X. Peng, H. Jiang, A. Lu and S. Yu, *IEEE Transactions on Computer-Aided Design of Integrated Circuits and Systems* **202**.
- [55] C. Lee, K. Noh, W. Ji, T. Gokmen, S. Kim, *Front Neurosci* **2021**, 15, 767953.

This article is protected by copyright. All rights reserved.

- [56] Z.-C. Zhang, Y. Li, J.-J. Wang, D.-H. Qi, B.-W. Yao, M.-X. Yu, X.-D. Chen, T.-B. Lu, *Nano Research* **2021**, 14, 4591.
- [57] T. Kim, S. Hu, J. Kim, J. Y. Kwak, J. Park, S. Lee, I. Kim, J.-K. Park, Y. Jeong, *Frontiers in Computational Neuroscience* **2021**, 15.
- [58] S. Walia, *Adv Mater Technol* **2022**, 7, 2101494.
- [59] H. Tian, Q. Guo, Y. Xie, H. Zhao, C. Li, J. J. Cha, F. Xia, H. Wang, *Adv. Mater.* **2016**, 28, 4991.
- [60] Y. Zhai, Y. Zhou, X. Yang, F. Wang, W. Ye, X. Zhu, D. She, W. D. Lu, S.-T. Han, *Nano Energy* **2019**, 67, 104262.
- [61] R. A. John, F. Liu, N. A. Chien, M. R. Kulkarni, C. Zhu, Q. Fu, A. Basu, Z. Liu, N. Mathews, *Adv Mater* **2018**, 30, 1800220.
- [62] H. K. He, R. Yang, W. Zhou, H. M. Huang, J. Xiong, L. Gan, T. Y. Zhai, X. Guo, *Small* **2018**, 14, 1.
- [63] C. S. Yang, D. S. Shang, N. Liu, G. Shi, X. Shen, R. C. Yu, Y. Q. Li, Y. Sun, *Adv. Mater.* **2017**, 29.
- [64] J. Zhu, Y. Yang, R. Jia, Z. Liang, W. Zhu, Z. U. Rehman, L. Bao, X. Zhang, Y. Cai, L. Song, R. Huang, *Adv Mater* **2018**, 30, e1800195.
- [65] Y. Wang, Z. Lv, J. Chen, Z. Wang, Y. Zhou, L. Zhou, X. Chen, S. T. Han, *Adv. Mater.* **2018**, 30, 1802883.
- [66] S. Qin, F. Wang, Y. Liu, Q. Wan, X. Wang, Y. Xu, Y. Shi, X. Wang, R. Zhang, *2D Mater.* **2017**, 4, 035022.
- [67] M. T. Sharbati, Y. Du, J. Torres, N. D. Ardolino, M. Yun, F. Xiong, *Adv. Mater.* **2018**, e1802353.

TOC

Artificial optoelectronic synaptic devices based on atomically thin large-area synthesised β - In_2S_3 nanosheets are presented. Intrinsic defects and vacancies in β - In_2S_3 induce persistent photocurrent under UV-visible wavelengths which is explored to imitate neural functions. Furthermore, the adoptability of these artificial synaptic devices for optoelectronic neuromorphic hardware is demonstrated.



Author Man

This article is protected by copyright. All rights reserved.